Investigations on the microstructural degradation and mechanical response of Ni–CGO anodes using phase-field method and stochastic modeling

Ahmed Elmoghazy[1*], Sabrina Weber[2], Ravi Kumar Jeela[3], Andreas Prahs[1,4], Benedikt Prifling[2], Daniel Schneider[1,3,4*], Volker Schmidt[2], Britta Nestler[1,3,4]

[1]Institute for Applied Materials - Microstructure Modelling and Simulation (IAM-MMS), Karlsruhe Institute of Technology (KIT), Straße am Forum 7, Karlsruhe, 76131, Germany.
[2]Institute of Stochastics, Ulm University, Helmholtzstraße 18, Ulm, 89069, Germany.
[3]Institute of Digital Materials Science (IDM), Karlsruhe University of Applied Sciences, Moltkestraße 30, Karlsruhe, 76133, Germany.
[4]Institute of Nanotechnology (INT), Karlsruhe Institute of Technology (KIT), Hermann-von-Helmholtz-Platz 1, Eggenstein-Leopoldshafen, 76344, Germany.

*Corresponding author(s). E-mail(s): ahmed.elmoghazy@kit.de; daniel.schneider@kit.edu;
Contributing authors: sabrina.weber@uni-ulm.de; ravi.jeela@partner.kit.edu; andreas.prahs@kit.edu; benedikt.prifling@uni-ulm.de; volker.schmidt@uni-ulm.de; britta.nestler@kit.edu;

Abstract

The microstructural degradation of Ni–CGO anodes in solid oxide fuel cells affects both electrochemical and mechanical properties. This study presents an automated workflow to quantify the evolution of geometrical descriptors and their influence on effective mechanical properties. Three-dimensional anode microstructures were aged up to 35,000 h using phase-field and stochastic modeling, followed by mechanical loading simulations. Aging caused microstructural coarsening as the mean pore diameter increased, while pore specific surface area and triple-phase boundary density decreased. Effective elastic moduli and the anisotropy index also decreased, indicating a mechanically weaker and less heterogeneous microstructure. The effective Hill modulus was strongly related to pore volume fraction and pore specific surface area. Average von Mises stress remained nearly constant, but the critical volume fraction increased with aging. It related with pore diameter and inversely with pore specific surface area and triple-phase boundary density.

Keywords: phase-field modeling, stochastic modeling, mechanical properties, electrochemical properties

1 Introduction

Motivation

Solid oxide fuel cells (SOFCs) are high-temperature electrochemical energy devices that efficiently convert fuel into electricity. Nickel/yttria-stabilized zirconia (Ni–YSZ) cermet anodes have been the state-of-the-art due to their good electrochemical performance and compatibility. Understanding how parameters like Ni/YSZ ratio, grain size, porosity, pore size distribution, tortuosity, and triple-phase boundary (TPB) density affect performance is key to optimizing these anodes [1]. However, Ni–YSZ anodes face challenges at lower operating temperatures (≈600°C) because YSZ's ionic conductivity drops, leading to a high polarization resistance [2]. To enable efficient operation at intermediate temperatures (500–700°C), alternative anode materials have emerged. In particular, nickel–gadolinium-doped ceria (Ni–CGO) cermet anodes have gained attention for intermediate-temperature SOFCs [3]. Gadolinium-doped ceria ($Ce_{0.9}Gd_{0.1}O_2$, CGO) offers higher ionic conductivity at these temperatures than YSZ and also exhibits mixed ionic-electronic conduction in reducing atmospheres [4]. This means that, unlike YSZ, the ceria phase can conduct both O^{2-} ions and electrons to some extent, so the fuel oxidation reaction is not limited to the narrow TPB regions, it can also occur on the broader CGO surface in the presence of gas (double-phase boundary of CGO and pore) [5]. Consequently, Ni–CGO anodes tend to have lower polarization resistance and high activity even at 600–700°C [4]. The mixed-conducting ceria phase also show tolerance to sulfur poisoning and coking, improving durability in realistic fuel conditions [2].

Degradation mechanisms in Ni-based anodes

During operation, SOFC anodes undergo microstructural evolution that can degrade performance over time. The Ni phase in Ni–CGO anodes is subject to similar degradation mechanisms as observed in Ni–YSZ anodes [6]. One primary mechanism is Ni coarsening (agglomeration). The Ni particles tend to sinter and grow in size under prolonged high-temperature reducing conditions. This coarsening reduces the overall Ni surface area and connectivity, and consequently diminishes the density of triple-phase boundary sites available for reaction [5]. For example, after long-term aging a Ni agglomeration can be observed, accompanied by a measurable decrease in TPB length density [7]. In Ni–CGO anodes aged for 240 hours at 800°C, the average Ni particle diameter was found to increase from 0.91 to 1.04 µm, with a corresponding drop in TPB density from 1.82 to 1.55 μm^{-2} [5].

Another major degradation mode is redox cycling damage. Nickel is highly susceptible to oxidation if air infiltrates the anode (e.g. during shut-down or fuel starvation) [8]. Upon oxidation to NiO, the Ni particles undergo a volumetric expansion of about 70% [9]. This large expansion/contraction during redox cycles imposes mechanical stresses that can crack the brittle ceramic scaffold and disrupt Ni–ceramic interfaces [10, 11]. For example, a study of Ni–YSZ anodes (analogous in structure to Ni–CGO) showed that after 20 redox cycles the TPB length was reduced by ≈ 77 % and new micro-cracks and pores had formed, contributing to a decrease in the hardness and the elastic modulus by 62 % and 45 %, respectively [10]. It is to be noted that this study focuses only on isothermal degradation due to particle coarsening, and not on redox cycling damage.

Studies on mechanical properties of Ni-based anodes

The anode is part of the load-bearing structure in many SOFC designs (especially anode-supported cells and metal-supported cells). Changes in its microstructure can affect its overall mechanical properties [12]. Despite extensive work on electrochemical performance and microstructural evolution in Ni–CGO anodes, direct, time-resolved measurements of the degradation of mechanical properties under steady, isothermal

aging remain scarce. The few Ni–CGO mechanical datasets that do exist are either single-state characterizations or geometry-specific tests: micro-/nano-indentation on Ni–CGO anode pellets and burst tests on NiO–CGO micro-tubes [13],biaxial flexure of electrolyte-supported laminates showing a strength drop when a NiO/CGO fuel electrode is added [14], flexural strength of NiO–CGO anode-supported cells fabricated by gel-casting [15], and in-situ synchrotron X-ray diffraction on Ni–CGO cermets that reveals lattice-scale thermo-mechanical behavior [16]. Designs emphasizing redox robustness of Ni–CGO also report improved mechanical stability under cycling, but these works target redox damage rather than isothermal coarsening [17]. Computational studies using reconstructed Ni–YSZ microstructures and porous-media models have further confirmed that elastic moduli decrease as porosity increases, consistent with Gibson–Ashby scaling laws [18–20]. To the best of our knowledge, no study has systematically tracked the directional elastic moduli or stress localization metrics of Ni–CGO as a function of isothermal aging time.

Originality

The literature establishes that Ni–CGO based anodes undergo microstructural degradation (e.g. Ni coarsening, TPB loss) and that the mechanical and electrochemical properties are generally strongly influenced by porosity and microstructural connectivity [21–23]. However, there is little investigations on how the elastic modulus of Ni–CGO anodes degrades with isothermal aging, whether it exhibits anisotropy, and how mechanical reliability metrics (e.g. stress distribution) correlate with evolving geometric descriptors. This study aims to fill this gap in the literature, and introduces a workflow that is capable of calculating different geometrical descriptors and effective mechanical properties.

Objective

In this study, we present a workflow implemented in Kadi4Mat [24, 25] to analyze aging Ni–CGO microstructures and quantify both geometrical and mechanical descriptors during aging. We investigate aging simulations carried out with the phase-field method [26–28] and compare it with stochastic microstructures [29]. The workflow calculates phase radii distributions, specific surface areas, double phase boundary, TPB density, and volume fractions. Furthermore, mechanical properties such as directional elastic moduli, Hill average for the elastic moduli, von Mises stress distributions, and the critical volume fraction (the volume fraction exceeding a stress threshold) are calculated. By comparing the temporal evolution of these descriptors and identifying dependencies, the aim is to provide new insight into the mechanical degradation of Ni–CGO anodes under isothermal aging, complementing the existing electrochemically focused literature.

Outline

In Sect. 2 the numerical models used to produce the aged microstructures are presented. The workflow is outlined and described in Sect. 3. The simulation studies and their results are discussed in Sect. 4. Concluding remarks are given in Sect. 5

2 Numerical Models

2.1 Physics-based simulations

Multiphase-field model

A modeling approach is employed to capture the essential physical mechanisms of coarsening in Ni-CGO anodes, along with maintaining computational efficiency. The model is based on the following assumptions: Conservation of mass and volume, isotropic interfacial properties, as well as surface and interfacial diffusion as dominant

mass transport pathways. Both Ni and CGO coarsening are considered primary degradation processes. Accordingly, this study focuses only on determining the effects of Ni and CGO coarsening on the microstructural evolution of the anode and, consequently, on the long-term performance of SOFCs.

A multiphase-field model centered on the grand-potential functional [30] together with a recent extension that accounts for surface self-diffusion [31], is adopted to model the coarsening phenomena of nickel and CGO. Model formulation includes the grand-potential functional Ω of the system with volume V, dependent on the order parameters $\boldsymbol{\phi} = \{\phi_1, \phi_2, \ldots, \phi_N\}$ of N phases and the volumetric chemical potentials $\boldsymbol{\mu} = \{\mu_1, \mu_2, \ldots, \mu_{K-1}\}$ of $K-1$ components and reads

$$\Omega(\boldsymbol{\phi}, \boldsymbol{\nabla\phi}, \boldsymbol{\mu}) = \int_V \frac{1}{\epsilon} w(\boldsymbol{\phi}) + \epsilon a(\boldsymbol{\nabla\phi}) + \psi(\boldsymbol{\phi}, \boldsymbol{\mu}) \, \mathrm{d}V. \tag{1}$$

Here, $w(\boldsymbol{\phi})$, $a(\boldsymbol{\nabla\phi})$ and $\psi(\boldsymbol{\phi}, \boldsymbol{\mu})$ represent the potential, gradient and bulk terms respectively. With the scalar parameter ϵ, the length scale is controlled and determines the diffuse interface width $\delta = \epsilon\pi^2/4$. The combined potential and gradient expressions according to the notation of [32] include the interfacial energy in the model and stabilize the interfacial profile with a finite thickness. The gradient term [26] is expressed as

$$a(\boldsymbol{\nabla\phi}) = -\sum_{\beta=2}^{N} \sum_{\alpha=1}^{\beta-1} \gamma_{\alpha\beta} \boldsymbol{\nabla}\phi_\alpha \cdot \boldsymbol{\nabla}\phi_\beta, \tag{2}$$

where $\gamma_{\alpha\beta}$ denotes the interfacial energy between phases α and β. An obstacle potential of the following form is chosen as

$$w(\boldsymbol{\phi}) = \begin{cases} \dfrac{16}{\pi^2} \displaystyle\sum_{\beta=2}^{N} \sum_{\alpha=1}^{\beta-1} \gamma_{\alpha\beta} \, \phi_\alpha \phi_\beta, & \boldsymbol{\phi} \in \mathcal{G}, \\ \infty, & \boldsymbol{\phi} \notin \mathcal{G}, \end{cases} \tag{3}$$

with Gibbs simplex $\mathcal{G} = \left\{ \displaystyle\sum_{\alpha=1}^{N} \phi_\alpha = 1 : \{\phi_\alpha \geq 0, \forall \alpha \in \{1, \ldots, N\}\} \right\}$.
Furthermore, the exact formulation of the bulk energy density is described in details in [5]. Following [26], the evolution equation of each phase-field ϕ_α is stated as

$$\epsilon \frac{\partial \phi_\alpha(x,t)}{\partial t} = \frac{1}{\tilde{N}} \sum_{\beta \neq \alpha}^{N} m_{\alpha\beta} \left(\frac{\delta\Omega}{\delta\phi_\beta} - \frac{\delta\Omega}{\delta\phi_\alpha} \right), \tag{4}$$

where $\tilde{N}$ denotes the local number of phases, $m_{\alpha\beta}$ (in $\mathrm{m}^4/(\mathrm{J}\cdot\mathrm{s})$) indicates the interface mobility of phases α and β. The terms $\delta/(\delta\phi_\alpha)$ and $\delta/(\delta\phi_\beta)$ correspond to the variational derivative with respect to ϕ_α and ϕ_β.

Three distinct order parameters $\boldsymbol{\phi} = \{\phi_{Ni}, \phi_{CGO}, \phi_{Pore}\}$ representing the nickel phase, the CGO phase, and the voids, respectively, are employed to model the porous Ni-CGO system. A set of two dimensionless composition variables $\boldsymbol{c} = \{c_{\mathrm{Ni}}, c_{\mathrm{CGO}}\}$ (mole fractions) with the composition of the porous phase $c_{\mathrm{Pore}} = 1 - c_{\mathrm{Ni}} - c_{\mathrm{CGO}}$ enable the transport of each substance. The dimensionless, conserved composition fields evolve according to the conservation laws governing the system, reading

$$\frac{\partial c_i(\boldsymbol{x},t)}{\partial t} = -\boldsymbol{\nabla} \cdot \boldsymbol{j}_i, \quad i = 1, \ldots, K-1 \tag{5}$$

in which $\boldsymbol{j}_i$ refers to the flux of the species i . The evolution of the chemical potential is given as

$$\frac{\partial \mu_i(\boldsymbol{x},t)}{\partial t} = \left[\sum_{\alpha=1}^{N}(\boldsymbol{\phi})\frac{\partial c_j^{\alpha}(\boldsymbol{\mu})}{\partial \mu_i}\right]^{-1}\left[\frac{\partial c_j(\boldsymbol{x},t)}{\partial t} - \sum_{\alpha=1}^{N} c_j^{\alpha}(\boldsymbol{\mu})\frac{\partial(\boldsymbol{\phi}(\boldsymbol{x},t))}{\partial t}\right]. \tag{6}$$

At the domain boundaries, zero-flux boundary conditions are imposed, whereby the boundaries are treated as isolating (i.e. $\boldsymbol{j_i}\cdot\boldsymbol{n}=0\forall i,\ x\in \mathrm{d}V$), with $\boldsymbol{n}$ denoting the normal to the domain boundary, implying no net flux across the boundary. Also, a perpendicular contact condition is assumed for the order parameters ($\boldsymbol{\nabla}\phi_\alpha\cdot\boldsymbol{n}=0$), which ensures boundary normality of the order parameter gradient. A SIMD-vectorized (Single instruction, multiple data) solver is used for the multiphase-field simulations, the implementation of which is described in detail in Section 4.2 of [33]. To minimize the effects of the attachment kinetics, the interfacial mobilities ($m_{\alpha\beta}$) are selected in such a way that the attachment kinetics remain insignificant, which is met by ensuring the characteristic length scale associated with the attachment kinetics, defined as ($l_c=\sqrt{B/(\gamma_{\alpha\beta}\,m_{\alpha\beta})}$) being much smaller than the diffuse interfacial width, i.e. ($l_c \ll \pi^2\epsilon/4$) [31].

Further details on the validation of the multiphase-field simulation results against experimental data of Ni-CGO anodes aged for 240 h, 1100 h and the model parameters, representing the operating conditions of Ni-CGO at 900 °C under a gas composition of H_2-50% / H_2O-50% can be found in [5, 34].

Solid mechanics formulation within the MPFM framework

The degradation of the elastic properties due to isothermal aging is one of the main objectives of the work at hand. Load simulations are carried out, accounting for the aged microstructure at distinct time increments. In this regard, a quasi-static solid mechanics formulation is employed, neglecting body forces. The balance of linear momentum is therefore expressed as

$$\mathrm{div}\,(\overline{\boldsymbol{\sigma}}) = \boldsymbol{0}, \quad \overline{\boldsymbol{\sigma}} = \sum_{\alpha=1}^{N^*}\phi_\alpha\boldsymbol{\sigma}^\alpha, \tag{7}$$

cf. [35], where $\overline{\boldsymbol{\sigma}}$ denotes the interpolated Cauchy stress calculated from the phase-specific stresses $\boldsymbol{\sigma}^\alpha$, and ϕ_α represents the order parameter of phase α. The infinitesimal strain tensor $\boldsymbol{\varepsilon}$ is interpolated analogously as

$$\boldsymbol{\varepsilon} = \sum_{\alpha=1}^{N^*}\phi_\alpha\boldsymbol{\varepsilon}^\alpha. \tag{8}$$

Following the jump condition approach [36–38], the local phase strain $\boldsymbol{\varepsilon}^\alpha$ can be written as

$$\boldsymbol{\varepsilon}^\alpha = \boldsymbol{\varepsilon} + \sum_{\beta=1,\beta\neq\alpha}^{N^*}\phi_\alpha\,{}^{\alpha\beta}[\![\boldsymbol{\varepsilon}]\!], \tag{9}$$

where ${}^{\alpha\beta}[\![\boldsymbol{\varepsilon}]\!]$ denotes the strain jump across diffuse interfaces between phases α and β given by ${}^{\alpha\beta}[\![\boldsymbol{\varepsilon}]\!] = \boldsymbol{\varepsilon}^\alpha - \boldsymbol{\varepsilon}^\beta$. Under the small strain assumption, the phase-specific strain $\boldsymbol{\varepsilon}^\alpha$ is decomposed additively into an elastic part $\boldsymbol{\varepsilon}^{\mathrm{el},\alpha}$ and a thermal expansion contribution $\boldsymbol{\varepsilon}^{\theta,\alpha}$,

$$\boldsymbol{\varepsilon}^{\alpha} = \boldsymbol{\varepsilon}^{\mathrm{el},\alpha} + \alpha_{\theta}^{\alpha} \Delta\theta \boldsymbol{I}, \tag{10}$$

with α_{θ}^{α} being the isotropic coefficient of thermal expansion of phase α, $\Delta\theta$ the temperature difference with respect to the reference temperature ($\Delta\theta = \theta - \theta_{\mathrm{ref}}^{\alpha}$), and $\boldsymbol{I}$ the second-order identity tensor.

The corresponding phase-specific stresses follow from Hooke's law in each phase,

$$\boldsymbol{\sigma}^{\alpha} = \mathbb{C}^{\alpha} \left[\boldsymbol{\varepsilon}^{\mathrm{el},\alpha}\right] = \mathbb{C}^{\alpha} \left[\boldsymbol{\varepsilon}^{\alpha} - \boldsymbol{\varepsilon}^{\theta,\alpha}\right], \tag{11}$$

where $\mathbb{C}^{\alpha}$ denotes the phase-specific stiffness tensor. Assuming isotropic elasticity for each phase, it is expressed as

$$\mathbb{C}^{\alpha} = 3K^{\alpha}\mathbb{P}_1 + 2G^{\alpha}\mathbb{P}_2, \tag{12}$$

with K^{α} and G^{α} representing the bulk and shear moduli, respectively. The projection tensors are defined as $\mathbb{P}_1 = 1/3\boldsymbol{I} \otimes \boldsymbol{I}$ and $\mathbb{P}_2 = \mathbb{I}^{\mathrm{S}} - \mathbb{P}_1$ where $\mathbb{I}^{\mathrm{S}}$ is the symmetric fourth-order identity tensor. The material properties used in this study are shown in Tab. 1.

Table 1: Material properties of the individual phases used in the mechanical simulations.

Phase	**Elastic modulus E (GPa)**	**Poisson's ratio ν**	**Thermal expansion α_θ ($\mathbf{K}^{-1}$)**
Ni	200 [39]	0.31 [39]	16.00×10^{-6} [40]
CGO	120 [41]	0.33 [41]	12.96×10^{-6} [42]

2.2 Stochastic simulations

Overview of the stochastic microstructure model

In this section, the stochastic microstructure model of [29] is briefly introduced. Therefore, two stochastically independent and motion invariant Gaussian random fields $\{X(t), t \in \mathbb{R}^3\}$ and $\{Y(t), t \in \mathbb{R}^3\}$ with covariance functions $\rho_X, \rho_Y : [0,\infty) \to \mathbb{R}$ are used. More precisely, the covariance functions are assumed to be $\rho_X(h) = \exp\big(-(\alpha_X h)^{\beta_X}\big)$ and $\rho_Y(h) = \exp\big(-(\alpha_Y h)^{\beta_Y}\big)$ for $h > 0$, where $\alpha_X, \alpha_Y \in (0,\infty)$ and $\beta_X, \beta_Y \in (0,2)$ [43]. In addition, we assume that X and Y are standardized, i.e., we assume that $\mathbb{E}X(t) = \mathbb{E}Y(t) = 0$ and $Var(X(t)) = Var(Y(t)) = 1$ for all $t \in \mathbb{R}^3$ However, a Gaussian random field is not suitable to accurately model the nickel phase of the considered SOFC anodes. That is why a χ^2-field $\{Z(t), t \in \mathbb{R}^3\}$ with two degrees of freedom based on the Gaussian field X is used. Formally, it holds $Z(t) = X_1^2(t) + X_2^2(t)$ for all $t \in \mathbb{R}^3$, where X_1 and X_2 are two independent copies of X. The covariance function of Z is then given by $\rho_Z(h) = 4\rho_X(h)^2$ for all $h > 0$ [44]. The two random fields Z and Y are used to model the three phases with so-called excursion sets [45]. Therefore, the two threshold parameters $\lambda_Z, \lambda_Y \in \mathbb{R}$ are used. More precisely, the model is given by

$$\begin{aligned} \Xi_{\mathrm{Ni}} &= \{t \in \mathbb{R}^3 : Z(t) \geq \lambda_Z\}, \\ \Xi_{\mathrm{P}} &= \mathrm{cl}(\{t \in \mathbb{R}^3 : Y(t) \geq \lambda_Y\} \cap \Xi_{\mathrm{Ni}}^{\complement}), \end{aligned}$$

$$\Xi_{\mathrm{GDC}} = \mathrm{cl}((\Xi_{\mathrm{Ni}} \cup \Xi_{\mathrm{P}})^{\complement}),$$

where *cl* denotes the topological closure and $\complement$ denotes the complement of a set. Note that the set Ξ_{Ni} models the nickel phase, while Ξ_{GDC} and Ξ_{P} model the GDC phase and pore space, respectively.

Parameters of the stochastic microstructure model

This stochastic microstructure model exhibits a six-dimensional parameter vector $\theta = (\lambda_Z, \lambda_Y, \alpha_X, \alpha_Y, \beta_X, \beta_Y)$, that is fitted with analytical formulas to the 3D microstructure obtained from the phase-field model simulations. More details on the fitting procedure can be found in [29]. Afterwards, an exponential regression is performed to each model parameter evolution over time, to obtain a time-dependent 3D microstructure model, see [29]. This time-dependent model is used to generate time series of the 3D microstructure of SOFC anodes. To ensure the continuity of the model realizations over time, a random seed is chosen and fixed afterwards for the entire time series. By setting a specific seed value, the pseudo-random number generator is initialized with a defined starting point, resulting in an identical sequence of random numbers each time the code is executed. Thus, the change in the microstructure over time is only influenced by the change in the model parameters.

3 Workflow

Overview

The workflow was implemented in KadiStudio, the workflow editor of the Kadi4Mat research data infrastructure. KadiStudio enables the design of modular, automated workflows that adhere to FAIR (Findable, Accessible, Interoperable, Reusable) data principles [25, 46]. A schematic overview of the developed workflow is shown in Fig.1, while the implementation in KadiStudio is illustrated in Fig.A1.

The workflow begins with importing aged microstructures, either from local storage or directly from the Kadi4Mat repository. After pre-processing, the microstructures are prepared for mechanical load simulations, which provide the effective stiffness and other effective properties. Subsequently, geometrical descriptors and performance-related metrics are computed. The resulting datasets are stored locally and uploaded to Kadi4Mat, ensuring long-term accessibility and reproducibility. This procedure is repeated for all microstructures under investigation.

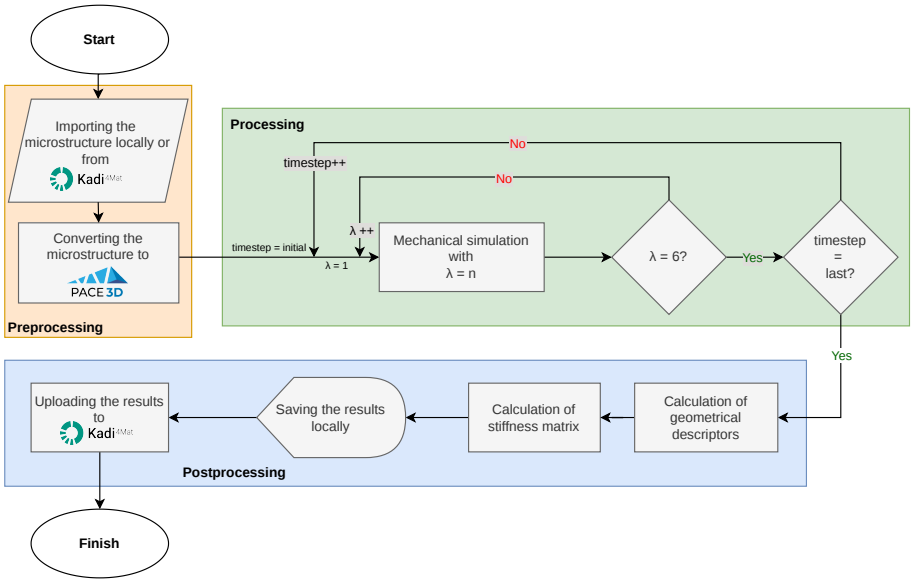

Fig. 1: Schematic representation of the workflow, implemented and used in this work, to run the mechanical simulations, calculate the geometrical descriptors and the effective mechanical properties.

3.1 Pre- and processing nodes

Preprocessing

The pre-processing stage of the workflow manages the import, preparation, and format conversion of microstructures for subsequent analysis. As illustrated in Fig. 1, the input nodes can access data from multiple sources, including local directories and the Kadi4Mat repository. The input data can both be aged and pristine microstructures.

Since the subsequent mechanical and geometrical analyses are executed within the Phase-field Algorithms for Computational Engineering (PACE3D) [47] environment [1], each imported dataset must first be converted to the PACE3D format. This is accomplished through a Python-based conversion script that reads the original data, typically provided as `.npy` arrays or `.tiff` image stacks, and transforms them into scalar fields compatible with the PACE3D software. During this step, the corresponding simulation input files are also generated automatically, defining the material parameters, phase identifiers, and boundary conditions required for the mechanical load simulations that follow.

Processing nodes

Once pre-processing is complete, the workflow advances to the processing stage, where the converted microstructures and their associated input files are passed to simulation nodes that perform the mechanical load calculations. For each aged microstructure, a loop over the temporal frames is executed, and within each frame, six independent uniaxial loading cases ($\lambda = 1, \ldots, 6$) are applied sequentially to compute the anisotropic elastic response of the material. An additional loading case is performed to extract further mechanical characteristics relevant to this study, such as the average von Mises stress and the critical volume fraction (Eq. 24). All simulations are performed using the PACE3D software. These simulations act as the basis for all subsequent analysis.

[1] formerly named as Parallel Algorithms for Crystal Evolution in 3D

3.2 Post-processing nodes

Geometrical descriptors

The workflow integrates methods to compute geometric descriptors of the microstructure, such as phase volume fractions, median particle diameter from the continuous particle size distribution, specific surface areas (SSAs), and triple phase boundary (TPB) density. Particle sizes are quantified using the continuous sphere-fitting method following Münch and Holzer [48], which fills the phase volume with overlapping spheres of varying diameters. This technique has been used successfully in experimental measurements of SOFC-anodes [49]. It provides the cumulative distribution that decreases from unity to zero as sphere diameter increases. The median particle size (d_{50}) is then defined at the 50% point of the cumulative distribution. TPB density is determined by a skeletonization algorithm that identifies intersection voxels, reduces them to a one-voxel-thick network, and smooths the resulting skeleton to minimize discretizations effects [50]. The SSA, A_α of a given phase α, is evaluated from its order parameter field ϕ_α by integrating the magnitude of its gradient over the simulation volume, i.e.

$$A_\alpha = \frac{1}{V} \int_V |\nabla \phi_\alpha| \, dV, \tag{13}$$

where V denotes the total volume. From these quantities, the interfacial areas $A_{\alpha-\beta}$ between different phase pairs (α, β) can be obtained by solving a linear system that relates the total surface area of each phase to the sum of its pairwise interfaces. For example, in a three-phase system consisting of Ni, CGO, and pores, the relations

$$A_{\mathrm{Ni}} = A_{\text{Ni-Pore}} + A_{\text{Ni-CGO}}, \tag{14a}$$
$$A_{\mathrm{CGO}} = A_{\text{CGO-Pore}} + A_{\text{Ni-CGO}}, \tag{14b}$$
$$A_{\mathrm{Pore}} = A_{\text{Ni-Pore}} + A_{\text{CGO-Pore}}, \tag{14c}$$

hold. Particular emphasis is placed on the CGO–pore interface. Owing to the mixed ionic–electronic conductivity of CGO, the entire CGO surface in contact with pores can participate in electrochemical reactions, making this descriptor highly relevant for electrical performance. All methods were implemented within the PACE3D framework and validated against established benchmarks [51].

Method of obtaining the directional elastic moduli

Since the fully resolved microstructure is available, a numerical homogenization is preferred over analytical mean field methods [52]. In this regard, the effective stiffness tensor $\bar{\mathbb{C}}$ is obtained by a strain-controlled numerical homogenization scheme based on six independent macroscopic load cases corresponding to the 6 components of the normed Voigt notation [53]. I.e., for $\lambda = 1, \ldots, 6$, a prescribed macroscopic strain vector $\bar{\boldsymbol{\varepsilon}}^\lambda$ is imposed in Voigt notation. For example, where $\lambda = 1$, the corresponding macroscopic strain vector has the amplitude ε_0 in the 11 direction. The corresponding boundary value problem of linear elasticity is solved yielding the stress field $\boldsymbol{\sigma}^\lambda(\mathbf{x})$. The volume-averaged macroscopic stress response is then computed as

$$\langle \boldsymbol{\sigma}^\lambda \rangle = \frac{1}{V} \int_V \boldsymbol{\sigma}^\lambda(\mathbf{x}) \, dV. \tag{15}$$

The homogenized constitutive relation can be expressed as $\langle \boldsymbol{\sigma}^\lambda \rangle = \bar{\mathbb{C}} \, \bar{\boldsymbol{\varepsilon}}^\lambda$. To extract the stiffness contributions from each load case, both sides are multiplied by $\underline{(\bar{\varepsilon}^\lambda)}^T$ and normalized by $\underline{(\bar{\varepsilon}^\lambda)}^T \underline{(\bar{\varepsilon}^\lambda)}$, which removes the dependence on the chosen strain

amplitude ε_0. This yields

$$\underline{\underline{\bar{C}}}^{\lambda} = \frac{\underline{\langle \sigma^{\lambda} \rangle}\, \underline{(\bar{\varepsilon}^{\lambda})}^{T}}{\underline{(\bar{\varepsilon}^{\lambda})}^{T}\, \underline{(\bar{\varepsilon}^{\lambda})}}. \tag{16}$$

Here, $\underline{\underline{\bar{C}}}$ denotes the matrix representation of the stiffness tensor $\mathbb{C}$ in normed Voigt notation. In this context, $\underline{\underline{\bar{C}}}^{\lambda}$ refers to the matrix representation of the λth column of $\underline{\underline{\bar{C}}}$ obtained by evaluating Eq. 16. Thus, each $\underline{\underline{\bar{C}}}^{\lambda}$ corresponds to a partial stiffness matrix that contributes a single column to $\bar{\mathbb{C}}$. For example, if the applied strain vector is $\underline{\bar{\varepsilon}}^{1} = [\,\varepsilon_0,\ 0,\ 0,\ 0,\ 0,\ 0\,]^{\mathsf{T}}$, then the averaged stress response $\langle \underline{\sigma}^{1} \rangle$ provides the first column of $\bar{\mathbb{C}}$. Analogously, shear load cases with $\underline{\bar{\varepsilon}}^{\lambda}$ nonzero in only one shear component contribute the corresponding shear columns, with the conventional $\sqrt{2}$ normalization [54].

The complete effective stiffness tensor is finally assembled as the sum of the contributions from the six load cases, i.e.,

$$\underline{\underline{\bar{C}}} = \sum_{\lambda=1}^{6} \underline{\underline{\bar{C}}}^{\lambda}. \tag{17}$$

Following Böhlke and Brüggermann [55], the elastic modulus body can be plotted from the homogenized stiffness tensor and the directional elastic moduli can be extracted therefrom [55] using

$$\frac{1}{E(\mathbf{d})} = \mathbf{d} \otimes \mathbf{d} \cdot \mathbb{S}[\mathbf{d} \otimes \mathbf{d}], \tag{18}$$

where $\mathbf{d}$ is the direction vector and $\mathbb{S}$ is the compliance matrix. This allows the calculation of the elastic moduli of any microstructure regardless of the material symmetry group.

In addition to these directional values, an isotropic equivalent modulus was computed by projecting the anisotropic tensor onto isotropic Voigt and Reuss bounds and averaging them in the sense of Hill [56]. The Voigt estimates for bulk and shear moduli are

$$K_{Voigt} = \frac{C_{11} + C_{22} + C_{33} + 2(C_{12} + C_{13} + C_{23})}{9}, \tag{19a}$$

$$G_{Voigt} = \frac{C_{11} + C_{22} + C_{33} - (C_{12} + C_{13} + C_{23}) + 3(C_{44} + C_{55} + C_{66})}{15}. \tag{19b}$$

while the Reuss bounds follow from the compliance tensor as

$$\frac{1}{K_{Reuss}} = S_{11} + S_{22} + S_{33} + 2(S_{12} + S_{13} + S_{23}), \tag{20a}$$

$$\frac{1}{G_{Reuss}} = \frac{4}{15}\big(S_{11} + S_{22} + S_{33} - S_{12} - S_{13} - S_{23}\big) + \frac{3}{15}(S_{44} + S_{55} + S_{66}). \tag{20b}$$

The Hill averages are then

$$K_{Hill} = \tfrac{1}{2}(K_{Voigt} + K_{Reuss}), \qquad G_{Hill} = \tfrac{1}{2}(G_{Voigt} + G_{Reuss}), \tag{21}$$

the effective isotropic elastic modulus is obtained as

$$E_{Hill} = \frac{9 K_{Hill} G_{Hill}}{3 K_{Hill} + G_{Hill}}. \tag{22}$$

It should be noted that these Voigt–Reuss–Hill estimates provide an isotropic projection of the generally anisotropic effective stiffness tensor, and are therefore used here only as scalar indicators to compare the overall stiffness level across aging states.

4 Results and discussions

Microstructures used

For the present analysis, six aged microstructures were considered. These include one aging simulation obtained with the MPFM, as well as five realizations generated by a stochastic reconstruction model to account for statistical variability. The phase-field simulation, originally reported in [5], was extended to a total aging time of 35,000 h and subsequently employed as input for calibrating the stochastic model parameters. This procedure has been described in details in Weber et al. [29]. Thus, the phase-field simulation offer a physical basis for understanding microstructural coarsening, whereas the stochastic realizations enhance the statistical assessment of the derived geometric and mechanical descriptors. The following sections present a systematic evaluation of these microstructures in terms of their geometrical characteristics and effective mechanical properties. For brevity, only the geometrical descriptors that are used in the subsequent evaluations in 4.3 are presented here.

4.1 Evolution of selected geometrical descriptors

Pore microstructural properties

Figure 2 summarizes the evolution of the three key pore descriptors during aging namely, volume fraction, mean diameter, and specific surface area. The pore volume fraction (Fig. 2a) remains within a narrow range throughout the aging process for both methods. In the phase-field simulation, which is calibrated with a free-energy coefficient to preserve phase volumes [31], the porosity stabilizes at approximately 36.6 %. The stochastic microstructures exhibit a wider spread across realizations, spanning roughly from 36.4 % to 37.0 %. While these variations are small in absolute terms, porosity directly reduces the load-bearing cross-section, so even modest differences could contribute to some scatter in the computed effective elastic properties. The porosity variations in the stochastic model remain far below variations encountered in redox cycling scenarios, where Ni oxidation to NiO induces approximately 70% volumetric expansion with severe consequences for mechanical integrity [10].

The mean pore diameter (Fig. 2b) increases monotonically, reflecting the coarsening of the pore network during aging. Both models show very similar values and trend characteristics: the average pore diameter grows from $\approx 0.65\,\mu m$ to approximately $0.86\,\mu m$ over the full aging duration. This coarsening is mirrored by a steady decline in the pore specific surface area (Fig. 2c), which decreases from $1.65\,\mu m^{-1}$ to $1.30-1.36\,\mu m^{-1}$. The steepest changes in both quantities occur within the first 5000 hours, after which the coarsening rate progressively diminishes. This decelerating trend is characteristic of diffusion-controlled Ostwald ripening, where the driving force for further coarsening decreases as the curvature differences between particles diminish [57].

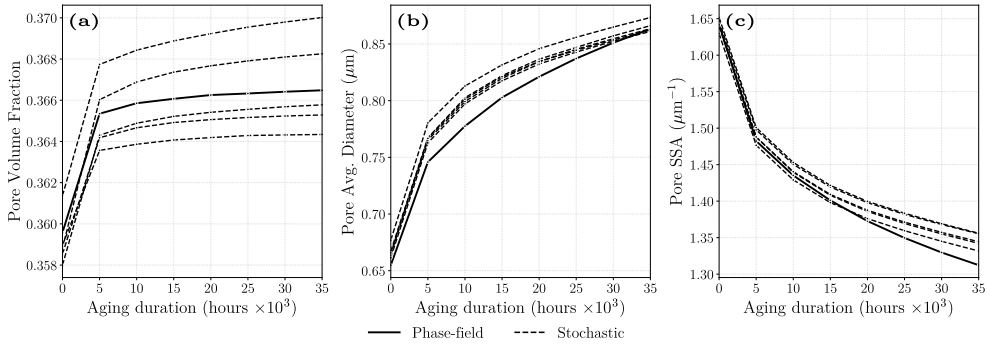

Fig. 2: Evolution of pore microstructural descriptors during aging for phase-field (solid lines) and the five realizations of the stochastic model (dashed lines): (a) volume fraction, (b) mean diameter, and (c) specific surface area.

Triple phase boundary density

The triple phase boundary density is one of the most critical descriptors for SOFC anodes, as it quantifies the length of lines where the three phases Ni, CGO, and pores coexist and thereby defines the number of classical electrochemical reaction sites [58]. As has been investigated in the literature [58–60], TPB density shows a pronounced decline during aging, shown in Fig. 3. In the phase-field simulation, TPB density decreases from an initial value of $2\,\mu m^{-2}$ to about $1.2\,\mu m^{-2}$, corresponding to a reduction of nearly 39 %. A similar trend is observed for the stochastic model realizations, where the initial values around $1.9\,\mu m^{-2}$ drop to around $1.08\,\mu m^{-2}$, amounting to a loss of roughly 43 %. This reduction closely mirrors the previously observed increases in mean particle diameter and decreases in SSA. This is consistent with previous consideration from the literature, where an increase in grain size leads to a decrease in the TPB density [61, 62]. From a functional perspective, the decline in TPB density directly translates into reduced electrochemical activity and higher polarization resistance [63]. A reduction of 40 - 43 % in TPB density implies that nearly half of the classical active sites vanish during the simulated aging, which is consistent with similar experimental reports [64].

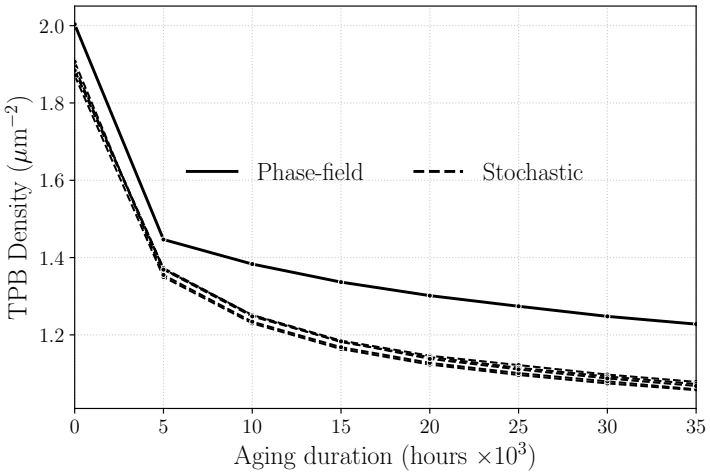

Fig. 3: Evolution of the triple phase boundary density during aging for the phase-field (solid line) and the five realizations of the stochastic model (dashed lines)

4.2 Effect of aging on effective mechanical properties

Elastic modulus

The boundary conditions and homogenization procedure for the determination of the effective directional elastic moduli and the Hill average are described in detail in Section 3.2.

Figure 4a shows the evolution of the directional elastic moduli for the phase-field microstructure. The initial response is notably anisotropic, where E_{zz} starts at approximately 62.5 GPa, while E_{xx} and E_{yy} begin at around 58 and 57 GPa, respectively. All three directions undergo a steep reduction within the first 5000 hours, after which E_{xx} and E_{yy} stabilize near 55 GPa – 55.5 GPa. The E_{zz} component continues to decrease more gradually, reaching approximately 57 GPa by 35,000 hours. As aging progresses, the three curves show signs of convergence, indicating that the initially anisotropic microstructure becomes increasingly isotropic through grain coarsening. The degree of elastic anisotropy can be quantified by the index

$$I_A = \frac{\max(E_{ii}) - \min(E_{ii})}{\langle E_{ii} \rangle}, \tag{23}$$

where $\langle E_{ii} \rangle$ is the average of the three directional elastic moduli. This normalized measure is used in various contexts to characterize directional stiffness variation, for instance in geological [65], biomedical [66], and fuel cell modeling applications [67]. As shown in Fig. 4b, the phase-field microstructure exhibits an initial anisotropy of $I_A \approx 0.09$, corresponding to a difference of nearly 9 % between the stiffest and softest loading directions. This value decreases progressively to approximately 0.03 by the end of the aging period, consistent with the convergence of the directional moduli observed in Fig. 4.

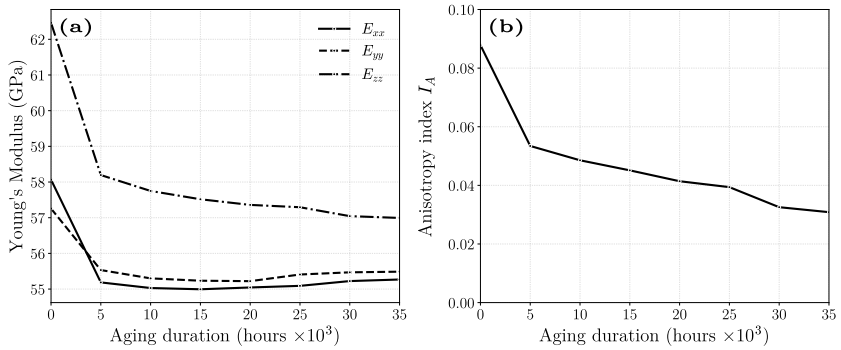

Fig. 4: Evolution of a) the directional elastic moduli E_{xx}, E_{yy} and E_{zz} and b) the anisotropy index I_A during aging for the phase-field microstructure.

The Hill average (Fig. 5) is considered as a single scalar measure for the effective elastic modulus and allows a direct comparison between the two modeling approaches. The stochastic realizations start with tightly clustered values around 43 GPa and decrease smoothly to 40 GPa – 39 GPa, corresponding to an average reduction of roughly 7 – 10 %. The phase-field microstructure begins at a lower value of approximately 41.5 GPa, drops rapidly to about 39 GPa ($\sim$ 6 % decrease) within the first 5000 hours, and then remains nearly constant. Thus, while both approaches capture the general stiffness loss during aging, the stochastic model predicts higher initial elastic modulus and a more gradual degradation, whereas the phase-field simulation exhibits a faster early reduction that saturates sooner. This discrepancy can be attributed to the slight variation in the pore volume fraction, as discussed above,

as well as the initial high degree of anisotropy inherent from the experimentally based structure. Such anisotropies are not included in the stochastic model, as discussed in [29]. Nevertheless, as coarsening progresses and the morphological differences between the experimentally derived and stochastically generated structures diminish, the Hill average elastic modulus starts to converge (∼39 GPa – 40 GPa).

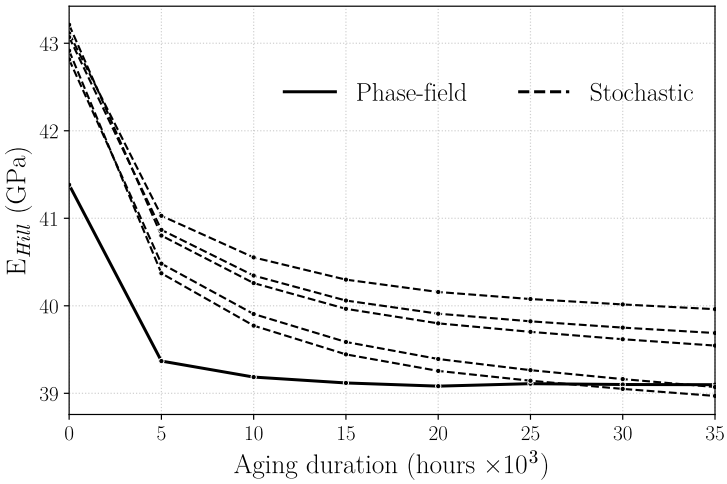

Fig. 5: Evolution of the Hill average elastic modulus during aging for the phase-field (solid line) and the five realizations of the stochastic model (dashed lines).

Mechanical boundary conditions for realistic operational scenario

To approximate the mechanical constraints experienced by the anode within a realistic SOFC stack, a boundary condition setup was applied. In this configuration, the anode–electrolyte interface was fixed in all displacement components $(u_x, u_y, u_z) = (0, 0, 0)$, as the anode is anchored to the electrolyte. The opposite surface, corresponding to the anode–interconnect interface, was constrained only in the normal direction ($u_z = 0$), preventing interpenetration with the metallic interconnect. The remaining lateral faces were restricted in displacement normal to their respective planes ($u_n = 0$) mimicking the mechanical confinement imposed by neighboring cells within the stack. Unlike the strain-controlled homogenization simulations used to compute the effective elastic moduli (Section 3.2), the stack configuration allows stress and strain fields to evolve naturally under combined mechanical confinement and thermal expansion, providing a more representative basis for assessing stress and strain distributions.

Average von Mises stress

The evolution of the average von Mises stress under the applied stack boundary conditions is shown in Fig. 6a. Here, the average von Mises stress is calculated as $\langle \sigma_{\mathrm{vM}} \rangle = \frac{1}{V} \int_V \sigma_{\mathrm{vM}}(\mathbf{x})\, dV$. Across all datasets, the values vary between 1.15–1.19 GPa (∼ 3.4 % difference) throughout the simulated aging period. Hence it can be assumed that the average von Mises stress is essentially constant throughout the 35,000 hours of aging. The absolute values given in this analysis are comparatively high because the simulations assume a purely elastic response without plasticity, creep, or fracture. In reality, stresses above the yield point would relax by inelastic mechanisms. Similar values have been reported in [68], where a theoretical model has been deployed to calculate the thermal compressive stresses arising due to the difference in thermal expansion coefficients between the Ni and CGO phases.

Critical volume fraction

While the average von Mises stress σ_{vm} shows small variation, the fraction of the microstructure experiencing stresses above a critical threshold $\sigma_{threshold}$ increases with aging, as shown in Fig. 6b. This quantity is here referred to as the critical volume fraction (CVF). It is calculated as

$$\mathrm{CVF} = \frac{1}{V_{\mathrm{tot}}} \int_{V(\sigma_{\mathrm{vM}} > \sigma_{\mathrm{threshold}})} dV. \tag{24}$$

A threshold $\sigma_{threshold}$ =1.19 GPa was chosen for this analysis, as this value corresponds to the upper limit of the average von Mises stress as shown in Fig. 6a. From a mechanical perspective, once a given fraction of the microstructure is driven above a critical threshold value, the likelihood of crack nucleation and interfacial decohesion increases. Thus, CVF provides an insight between microstructural aging and the probability of mechanical failure. The CVF rises from about 0.325 initially to 0.364 in the aged state throughout all microstructures. The increasing CVF indicates that aging promotes a redistribution of stress rather than an overall rise in the global stress level (as evident by the nearly constant average von Mises levels). As the microstructure coarsens, some areas become less stressed because local curvatures smooth out or small features disappear, while other areas carry a greater portion of the load. Consequently, even though the overall average von Mises stress stays nearly constant, a larger fraction of the material volume experiences stresses above the critical threshold.

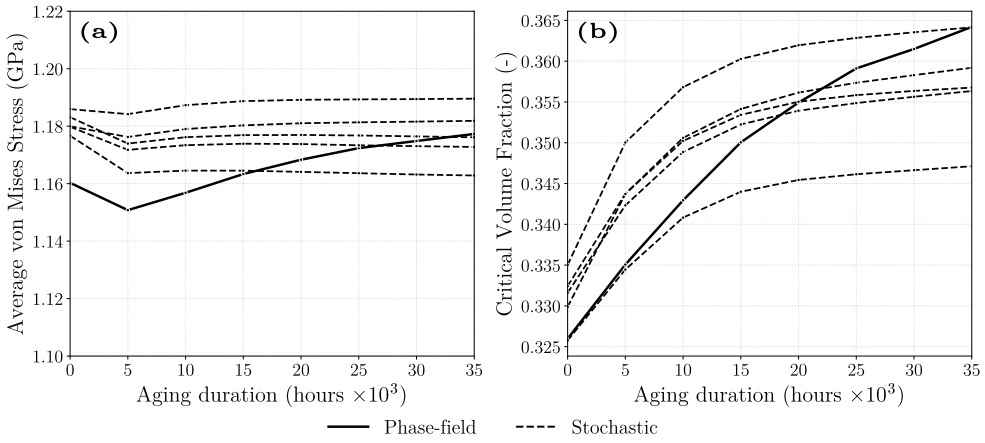

Fig. 6: Evolution of a) the average von Mises stress, and b) the critical volume fraction during aging for the phase-field (solid lines) and the five realizations of the stochastic model (dashed lines).

4.3 Relating microstructure geometry and mechanical properties

Remark

To better understand how microstructural degradation relates to mechanical performance, pairwise relationships between geometrical descriptors and mechanical properties were analyzed. The considered geometrical descriptors are particle radii, specific surface areas (SSAs), TPB density, and specific pairwise contact areas, while the mechanical quantities include the directional elastic moduli, Hill average elastic modulus, the average von Mises stress, and the critical volume fraction (CVF). For reasons of brevity, only relationships that exhibit clear trends and allow for a consistent physical interpretation are presented below, whereas relationships showing no

discernible trend or being dominated by scatter are omitted. Consequently, the following discussion focuses on Hill average elastic modulus and the CVF. The average von Mises stress is not considered further, as it remains nearly constant under the chosen boundary conditions and therefore does not yield meaningful trends with the evolving microstructure.

As the objective of this section is to identify general relationships rather than method-specific differences, no distinction is made between phase-field and stochastic microstructures. Instead, all data points are treated as a single pooled dataset. The relationships shown below were quantified by least-squares regression. Depending on the observed trend, either a linear regression or a second-degree polynomial regression was applied. The deviations reported below correspond to the maximum positive and negative relative deviations from the fitted curve and are defined (in %) as

$$\delta_i = 100 \times \frac{y_i - \hat{y}_i}{\hat{y}_i}, \tag{25}$$

where y_i denotes the computed value and $\hat{y}_i$ the corresponding value predicted by the regression model.

Elastic modulus

Establishing a relation between the Hill average elastic modulus E_{Hill} and the microstructural descriptors provides a direct link between mechanical stiffness and geometric coarsening. Figure 7 shows that E_{Hill} decreases approximately linearly with increasing pore volume fraction. While the pore fraction variations observed during aging are relatively small (around 1.5% across all data, cf. Section 4.1), these modest changes are already associated with measurable reductions in E_{Hill}. This is consistent with other homogenization schemes (e.g. Voigt homogenization), according to which the phase volume fractions contribute directly to the effective elastic response. The relationship is consistent across datasets, with relative deviations δ_i within $-1.9\,\%$ and $3.3\,\%$. This sensitivity reflects the strong role of porosity in reducing the effective load-bearing cross-section, consistent with previous studies on porous SOFC anodes [10, 19].

Additionally, the Hill average modulus increases with the specific surface area of the pore phase. This relationship is well captured by a second-degree polynomial fit, with δ_i between $-3.2\,\%$ and $1.8\,\%$. A higher pore SSA corresponds to a finer, more distributed pore network, whereas a lower SSA indicates that the pore space has coarsened into fewer, larger voids. As pores coarsen, the surrounding solid phases lose interfacial contact area and local load-transfer paths are disrupted. Conversely, a finer pore morphology preserves a more continuous and well-connected solid skeleton. The pore SSA thus serves as an indirect measure of the connectivity of the Ni–CGO network. Its decrease during aging reflects not only pore coarsening itself, but also the accompanying degradation of the solid-phase connectivity. Even though the Ni volume fraction remains nearly constant, the (distinct) decrease of the effective Young's modulus is attributed to the increase of the pore volume fraction.

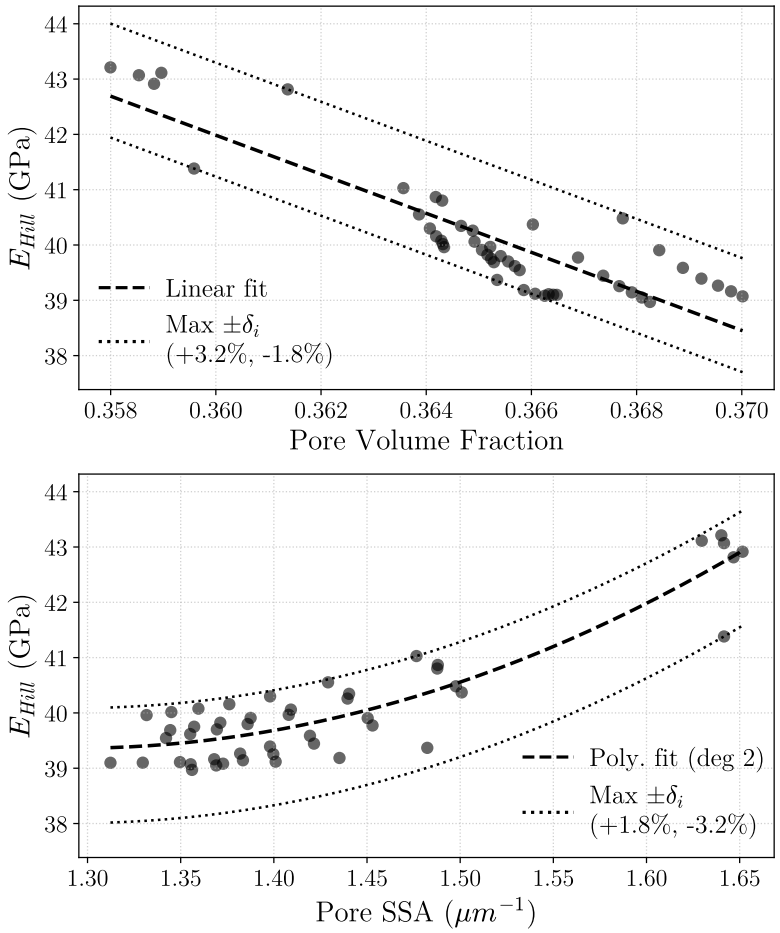

Fig. 7: Relationship between the Hill average elastic modulus (E_{Hill}) and the pore phase volume fraction (top), and the specific surface area of the pore phase (bottom).

Critical volume fraction

The critical volume fraction — representing the volume fraction exceeding a von Mises stress of 1.2 GPa — exhibits a strong dependence on the geometric characteristics of the pore phase, as well as on the TPB density. As shown in Fig. 8 (top and middle rows), CVF increases nearly linearly with the mean pore diameter, while it decreases correspondingly with SSA of the pore phase. The mean pore diameter exhibits a clear relationship with the CVF across all simulations, with relative deviations δ_i between $-3.0\,\%$ and $1.9\,\%$. The SSA of the pore phase shows a similar but opposite trend, with δ_i ranging from $-2.7\,\%$ to $2.1\,\%$. Consequently, these opposing trends are manifestations of the morphological transformation due to pore coarsening. Furthermore, a negative relationship is observed between the CVF and the TPB density, with relative deviations δ_i between $-3.7\,\%$ and $3.5\,\%$ across all datasets (Fig. 8, bottom row). This trend indicates that microstructures possessing higher TPB density, i.e., a finer and more interconnected phase arrangement, exhibit a lower volume of material that exceeds the critical stress threshold. From a mechanical perspective, TPB density acts as a quantitative descriptor of microstructural fineness and phase interpenetration. As the TPB network deteriorates through coarsening and interface loss, the critical volume fraction increases.

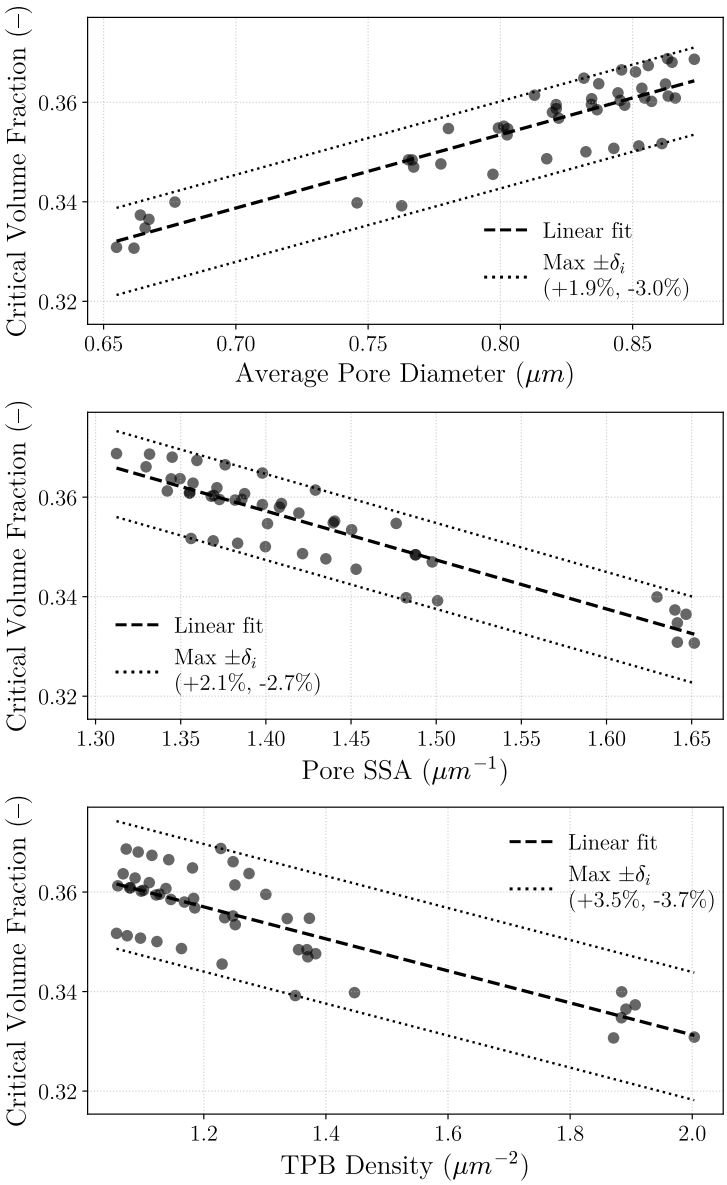

Fig. 8: Relationship between the critical volume fraction and the average pore diameter (top), the specific surface area of the pore phase (middle) and the triple phase boundary density (bottom).

5 Concluding remarks

This work presented a fully automated and FAIR-compliant workflow for analyzing the morphological and mechanical evolution of Ni–CGO anodes, implemented in KadiStudio within the Kadi4Mat infrastructure [24]. The workflow imports the microstructure locally or from the Kadi4Mat repository, runs mechanical simulation, and computes the geometrical descriptors as well as the effective mechanical properties of the microstructure. The results and metadata are uploaded into Kadi4Mat repository for reproducibility. One microstructure reconstructed from real Ni-CGO anode image data aged till 35,000 hours [5] using the multiphase-field method and five realizations of the stochastic model outlined in [29] were investigated. The geometrical analysis revealed that phase fractions remain essentially constant during aging, confirming that degradation is driven primarily by interface reduction rather

than bulk volume change. Coarsening manifests as an increase in the mean particle diameter and a decrease in specific surface area, triple phase boundary density, and interfacial (CGO/Pore) contact area. Numerical homogenization revealed a reduction in the effective stiffness, quantified through the directional elastic modulus and the Hill average modulus. The anisotropy index further showed that the initially anisotropic microstructure, used for the phase-field simulations, evolves toward a more isotropic state as aging proceeds. This reduction in stiffness was consistent across all datasets and showed a clear relationship with the of specific surface area of the pore phase, highlighting that microstructural fineness and pore network connectivity play a role in the effective mechanical behavior. Under the stack boundary conditions representing anode confinement within the SOFC assembly, the spatial stress distribution, arising due to thermal expansion, displayed distinct behavior. As the average von Mises stress remained nearly constant due to the macroscopic boundary constraints, the volume fraction exceeding a critical stress threshold increased with time. This increase in critical volume fraction reflects a stress redistribution, as a higher fraction of the microstructure experiences higher stresses. The critical volume fraction was found to relate to the average pore diameter, and inversely with triple phase boundary density and specific surface area of the pore phase. Thus, the critical volume fraction directly links microstructural degradation to mechanical weakening and simultaneously connects electrochemical and mechanical descriptors. These results demonstrate that microstructural coarsening in Ni–CGO anodes not only reduces electrochemically active interfaces (hence, electrochemical performance degrades) but also degrades effective mechanical properties of the anode. Overall, the findings and microstructure-property-relationships establish a solid basis for advancing electrode material optimization by enabling the design of microstructures with minimized degradation susceptibility. The established workflow enables such coupled analyses to be performed automatically and reproducibly, with results and metadata stored in Kadi4Mat for future reuse.

Acknowledgments. The authors would like to thank the Federal Ministry of Research, Technology and Space (BMFTR) for financial support within the priority program "Mathematics for Innovations" in the framework of "DASEA-4-SOFC" (grant number 05M2022). The financial support of the MTET programme (no. 38.02.01) of Helmholtz association is gratefully acknowledged. The authors acknowledge support by the state of Baden-Württemberg through bwHPC.

Declaration of generative AI and AI-assisted technologies in the manuscript preparation process. During the preparation of this work the author used ChatGPT 5.4 in order to assist with language editing and improve readability. After using this tool, the author reviewed and edited the content as needed and takes full responsibility for the content of the published article.

Appendix A Workflow in KadiStudio

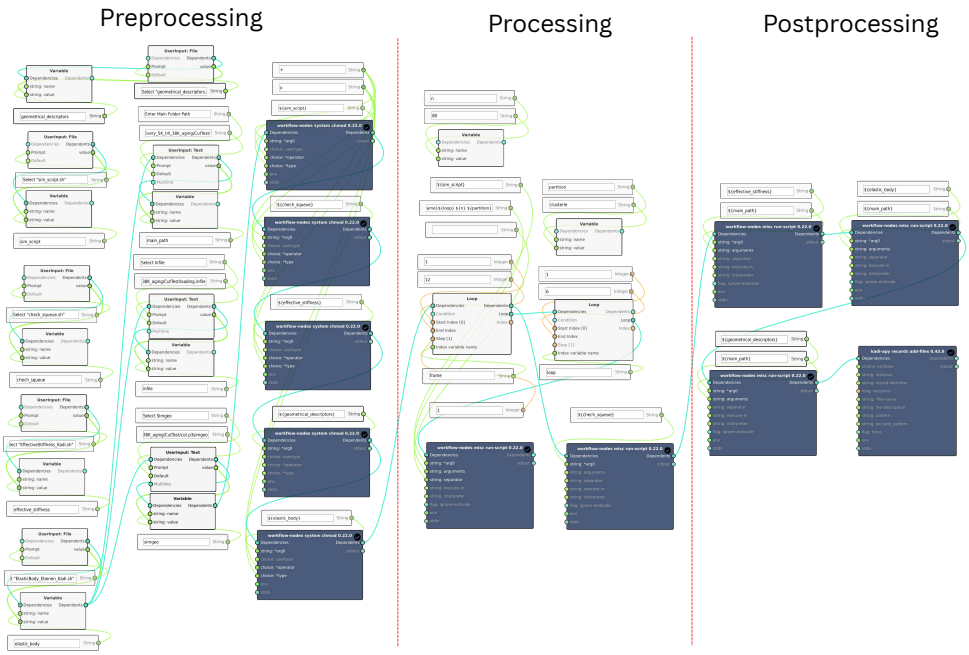

Fig. A1: A screenshot from KadiStudio showing the implemented workflow

References

[1] Vafaeenezhad S, Hanifi AR, Laguna-Bercero MA, Etsell TH, Sarkar P. Microstructure and long-term stability of Ni–YSZ anode supported fuel cells: a review. Materials Futures. 2022;1(4):042101. https://doi.org/10.1088/2752-5724/ac88e7.

[2] Liu Y, Juckel M, Menzler NH, Weber A. Ni/GDC fuel electrode for low-temperature SOFC and its aging behavior under accelerated stress. Journal of The Electrochemical Society. 2024;171(5):054514. https://doi.org/10.1149/1945-7111/ad4917.

[3] Vinchhi P, Khandla M, Chaudhary K, Pati R. Recent advances on electrolyte materials for SOFC: A review. Inorganic Chemistry Communications. 2023;152:110724. https://doi.org/10.1016/j.inoche.2023.110724.

[4] Nenning A, Bischof C, Fleig J, Bram M, Opitz AK. The relation of microstructure, materials properties and impedance of SOFC electrodes: A case study of Ni/GDC anodes. Energies. 2020;13(4):987. https://doi.org/10.3390/en13040987.

[5] Jeela RK, Tosato G, Ahmad M, Wieler M, Koeppe A, Nestler B, et al. Enhancing solid oxide fuel cells development through Bayesian Active Learning. Advanced Energy Materials. 2025;15(34). https://doi.org/10.1002/aenm.202501216.

[6] Sciazko A, Shimura T, Komatsu Y, Shikazono N. Ni-GDC and Ni-YSZ electrodes operated in solid oxide electrolysis and fuel cell modes. Journal of Thermal Science and Technology. 2021;16(1):JTST0013–JTST0013. https://doi.org/10.1299/jtst.2021jtst0013.

[7] Zekri A, Knipper M, Parisi J, Plaggenborg T. Microstructure degradation of Ni/CGO anodes for solid oxide fuel cells after long operation time using 3D reconstructions by FIB tomography. Physical Chemistry Chemical Physics. 2017;19(21):13767–13777. https://doi.org/10.1039/c7cp02186k.

[8] Klemensø T, Mogensen M. Ni–YSZ solid oxide fuel cell anode behavior upon redox cycling based on electrical characterization. Journal of the American Ceramic Society. 2007;90(11):3582–3588. https://doi.org/10.1111/j.1551-2916.2007.01909.x.

[9] Faes A, Nakajo A, Hessler-Wyser A, Dubois D, Brisse A, Modena S, et al. RedOx study of anode-supported solid oxide fuel cell. Journal of Power Sources. 2009;193(1):55–64. https://doi.org/10.1016/j.jpowsour.2008.12.118.

[10] Song B, Ruiz-Trejo E, Bertei A, Brandon NP. Quantification of the degradation of Ni-YSZ anodes upon redox cycling. Journal of Power Sources. 2018;374:61–68. https://doi.org/10.1016/j.jpowsour.2017.11.024.

[11] Ettler M, Timmermann H, Malzbender J, Weber A, Menzler NH. Durability of Ni anodes during reoxidation cycles. Journal of Power Sources. 2010;195(17):5452–5467. https://doi.org/10.1016/j.jpowsour.2010.03.049.

[12] Basu R, Kumar SS, Mukhopadhyay AK, Maiti HS. Improvement in mechanical properties of anode-supported planar SOFC. ECS Transactions. 2007;7(1):533–541. https://doi.org/10.1149/1.2729133.

[13] Roy BR, Sammes NM, Suzuki T, Funahashi Y, Awano M. Mechanical properties of micro-tubular solid oxide fuel cell anodes. Journal of Power Sources. 2009;188(1):220–224. https://doi.org/10.1016/j.jpowsour.2008.11.076.

[14] Masini A, Strohbach T, Šiška F, Chlup Z, Dlouhý I. Electrolyte-supported fuel cell: Co-sintering effects of layer deposition on biaxial strength. Materials. 2019;12(2):306. https://doi.org/10.3390/ma12020306.

[15] Morales M, Laguna-Bercero MA, Jiménez-Piqué E. Direct-methane anode-supported solid oxide fuel cells fabricated by aqueous gel-casting. Journal of the European Ceramic Society. 2023;43(7):2740–2751. https://doi.org/10.1016/j.jeurceramsoc.2022.06.027.

[16] Heenan TMM, Robinson JB, Lu X, Tjaden B, Cervellino A, Bailey JJ, et al. Understanding the thermo-mechanical behaviour of solid oxide fuel cell anodes using synchrotron X-ray diffraction. Solid State Ionics. 2018;314:156–164. https://doi.org/10.1016/j.ssi.2017.10.025.

[17] Park JH, Lee JH, Yoon KJ, Kim H, Ji HI, Yang S, et al. A nanoarchitectured cermet composite with extremely low Ni content for stable high-performance solid oxide fuel cells. Acta Materialia. 2021;206:116580. https://doi.org/10.1016/j.actamat.2020.116580.

[18] Gibson LJ, Ashby MF. Cellular Solids: Structure and Properties. Cambridge University Press; 1997.

[19] Pihlatie M, Kaiser A, Mogensen M. Mechanical properties of NiO/Ni–YSZ composites depending on temperature, porosity and redox cycling. Journal of the European Ceramic Society. 2009;29(9):1657–1664. https://doi.org/10.1016/j.jeurceramsoc.2008.10.017.

[20] Pabst W, Gregorová E, Tichá G. Elasticity of porous ceramics - A critical study of modulus porosity relations. Journal of the European Ceramic Society. 2006;26(7):1085–1097. https://doi.org/10.1016/j.jeurceramsoc.2005.01.041.

[21] Chen Z, Wang X, Giuliani F, Atkinson A. Analyses of microstructural and elastic properties of porous SOFC cathodes based on focused ion beam tomography. Journal of Power Sources. 2015;273:486–494. https://doi.org/10.1016/j.jpowsour.2014.09.131.

[22] Liu L, Kim GY, Chandra A. Modeling of Ni–CGO anode in a solid oxide fuel cell deposited by spray pyrolysis. Journal of Power Sources. 2012;210:129–137. https://doi.org/10.1016/j.jpowsour.2012.03.031.

[23] Lu X, Heenan TMM, Bailey JJ, Li T, Li K, Brett DJL, et al. Correlation between triple phase boundary and the microstructure of Solid Oxide Fuel Cell anodes: The role of composition, porosity and Ni densification. Journal of Power Sources. 2017;365:210–219. https://doi.org/10.1016/j.jpowsour.2017.08.095.

[24] Brandt N, Griem L, Herrmann C, Schoof E, Tosato G, Zhao Y, et al. Kadi4Mat: A research data infrastructure for materials science. Data Science Journal. 2021;20:8. https://doi.org/10.5334/dsj-2021-008.

[25] Griem L, Zschumme P, Laqua M, Brandt N, Schoof E, Altschuh P, et al. KadiStudio: FAIR modelling of scientific research processes. Data Science Journal. 2022;21. https://doi.org/10.5334/dsj-2022-016.

[26] Steinbach I, Pezzolla F. A generalized field method for multiphase transformations using interface fields. Physica D: Nonlinear Phenomena. 1999;134(4):385–393. https://doi.org/10.1016/S0167-2789(99)00129-3.

[27] Nestler B, Choudhury A. Phase-field modeling of multi-component systems. Current Opinion in Solid State and Materials Science. 2011;15(3):93–105. https://doi.org/10.1016/j.cossms.2011.01.003.

[28] Prahs A, Schneider D, Nestler B. A continuum thermodynamic approach to the phase-field method: the order parameter as internal state variable. Continuum Mechanics and Thermodynamics. 2025;37(4):55. https://doi.org/10.1007/s00161-025-01383-y.

[29] Weber S, Prifling B, Jeela RK, Prahs A, Schneider D, Nestler B, et al. A time-continuous approach to analyzing anode aging in solid-oxide fuel cells via stochastic 3D microstructure modeling and physics-based simulations. Computational Materials Science. 2026;264:114491. https://doi.org/10.1016/j.commatsci.2026.114491.

[30] Choudhury A, Nestler B. Grand-potential formulation for multicomponent phase transformations combined with thin-interface asymptotics of the double-obstacle potential. Phys Rev E. 2012;85(2):021602. https://doi.org/10.1103/PhysRevE.85.021602.

[31] Hoffrogge PW, Mukherjee A, Nani ES, Amos PGK, Wang F, Schneider D, et al. Multiphase-field model for surface diffusion and attachment kinetics in the grand-potential framework. Physical Review E. 2021;103(3):033307. https://doi.org/10.1103/PhysRevE.103.033307.

[32] Nestler B, Garcke H, Stinner B. Multicomponent alloy solidification: phase-field modeling and Simulations. Phys Rev E. 2005;71(4):041609. Publisher: American

Physical Society. https://doi.org/10.1103/PhysRevE.71.041609.

[33] Seiz M, Hoffrogge P, Hierl H, Reiter A, Schneider D, Nestler B. In: Phase-Field simulations with the grand potential approach. Springer International Publishing; 2021. p. 561–577.

[34] Jeela RK, Ahmad M, Wieler M, Liu Y, Juckel M, Schneider D, et al. Multiphase-field simulation studies of coarsening in Ni-GDC SOFC anode microstructures and the effect of interfacial energies. ACS Applied Energy Materials. 2025;p. 17670–17687. https://doi.org/10.1021/acsaem.5c02218.

[35] Schneider D, Tschukin O, Choudhury A, Selzer M, Böhlke T, Nestler B. Phase-field elasticity model based on mechanical jump conditions. Computational Mechanics. 2015;55(5):887–901. https://doi.org/10.1007/s00466-015-1141-6.

[36] Durga A, Wollants P, Moelans N. Evaluation of interfacial excess contributions in different phase-field models for elastically inhomogeneous systems. Modelling and Simulation in Materials Science and Engineering. 2013;21(5):055018. https://doi.org/10.1088/0965-0393/21/5/055018.

[37] Mosler J, Shchyglo O, Montazer Hojjat H. A novel homogenization method for phase field approaches based on partial rank-one relaxation. Journal of the Mechanics and Physics of Solids. 2014;68:251–266. https://doi.org/10.1016/j.jmps.2014.04.002.

[38] Schneider D, Schwab F, Schoof E, Reiter A, Herrmann C, Selzer M, et al. On the stress calculation within phase-field approaches: A model for finite deformations. Comput Mech. 2017;60(2):203–217. https://doi.org/10.1007/s00466-017-1401-8.

[39] Farraro R, Mclellan RB. Temperature dependence of the Young's modulus and shear modulus of pure nickel, platinum, and molybdenum. Metallurgical Transactions A. 1977;8(10):1563–1565. https://doi.org/10.1007/bf02644859.

[40] Hidnert P. Thermal expansion of some nickel alloys. Journal of Research of the National Bureau of Standards. 1957;58(2):89–92.

[41] Fan X, Case ED, Yang Q, Nicholas JD. Room temperature elastic properties of gadolinia-doped ceria as a function of porosity. Ceramics International. 2013;39(6):6877–6886. https://doi.org/10.1016/j.ceramint.2013.02.022.

[42] Andersen KB, Charlas B, Stamate E, Hansen KK. Permeability, strength and electrochemical studies on ceramic multilayers for solid-state electrochemical cells. Heliyon. 2017;3(8):e00371. https://doi.org/10.1016/j.heliyon.2017.e00371.

[43] Lantuéjoul C. Geostatistical Simulation: Models and Algorithms. Springer; 2013.

[44] Chiu SN, Stoyan D, Kendall WS, Mecke J. Stochastic Geometry and Its Applications. 3rd ed. John Wiley & Sons; 2013.

[45] Molchanov I. Theory of Random Sets. Springer; 2005.

[46] Draxl C, Scheffler M. In: Big Data-Driven Materials Science and Its FAIR Data Infrastructure. Springer International Publishing; 2020. p. 49–73.

[47] Hötzer J, Reiter A, Hierl H, Steinmetz P, Selzer M, Nestler B. The parallel multi-physics phase-field framework Pace3D. J Comput Sci. 2018;26:1–12. Publisher: Elsevier BV. https://doi.org/10.1016/j.jocs.2018.02.011.

[48] Münch B, Holzer L. Contradicting geometrical concepts in pore size analysis attained with electron microscopy and mercury intrusion. Journal of the American Ceramic Society. 2008;91(12):4059–4067. https://doi.org/10.1111/j.1551-2916.2008.02736.x.

[49] Holzer L, Iwanschitz B, Hocker T, Münch B, Prestat M, Wiedenmann D, et al. Microstructure degradation of cermet anodes for solid oxide fuel cells: Quantification of nickel grain growth in dry and in humid atmospheres. Journal of Power Sources. 2011;196(3):1279–1294. https://doi.org/10.1016/j.jpowsour.2010.08.017.

[50] Palàgyi K, Kuba A. A 3D 6-subiteration thinning algorithm for extracting medial lines. Pattern Recognition Letters. 1998;19(7):613–627. https://doi.org/10.1016/s0167-8655(98)00031-2.

[51] Hoffrogge PW, Schneider D, Wankmüller F, Meffert M, Gerthsen D, Weber A, et al. Performance estimation by multiphase-field simulations and transmission-line modeling of nickel coarsening in FIB-SEM reconstructed Ni-YSZ SOFC anodes I: Influence of wetting angle. Journal of Power Sources. 2023;570:233031. https://doi.org/10.1016/j.jpowsour.2023.233031.

[52] Kehrer L, Pinter P, Böhlke T. Mean and full field homogenization of artificial long fiber reinforced thermoset polymers. PAMM. 2017;17(1):603–604. https://doi.org/10.1002/pamm.201710271.

[53] Bertram A, Glüge R. Solid Mechanics: Theory, Modeling, and Problems. Springer International Publishing; 2015.

[54] Bertram A. Elasticity and Plasticity of Large Deformations: Including Gradient Materials. Springer International Publishing; 2021.

[55] Böhlke T, Brüggemann C. Graphical Representation of the Generalized Hooke's Law. Technische Mechanik - European Journal of Engineering Mechanics. 2019;21(2):145–158.

[56] Hill R. The elastic behaviour of a crystalline aggregate. Proceedings of the Physical Society Section A. 1952;65(5):349–354. https://doi.org/10.1088/0370-1298/65/5/307.

[57] Mullins W. Grain boundary grooving by volume diffusion. Transactions of the American Institute of Mining and Metallurgical Engineers. 1960;218(2):354–361.

[58] Kenney B, Valdmanis M, Baker C, Pharoah JG, Karan K. Computation of TPB length, surface area and pore size from numerical reconstruction of composite solid oxide fuel cell electrodes. Journal of Power Sources. 2009;189(2):1051–1059. https://doi.org/10.1016/j.jpowsour.2008.12.145.

[59] Nerat M. A model of solid oxide fuel cell degradation on a microstructural level. Applied Sciences. 2020;10(6):1906. https://doi.org/10.3390/app10061906.

[60] Hoffrogge PW, Daubner S, Schneider D, Nestler B, Zhou B, Eiken J. Triple junction benchmark for multiphase-field models combining capillary and bulk driving forces. Modelling and Simulation in Materials Science and Engineering. 2024;33(1):015001. https://doi.org/10.1088/1361-651x/ad8d6f.

[61] Deng X, Petric A. Geometrical modeling of the triple-phase-boundary in solid oxide fuel cells. Journal of Power Sources. 2005;140(2):297–303. https://doi.org/10.1016/j.jpowsour.2004.08.046.

[62] Timurkutluk B, Ciflik Y, Altan T, Genc O. Synthetical designing of solid oxide fuel cell electrodes: Effect of particle size and volume fraction. International Journal of Hydrogen Energy. 2022;47(73):31446–31458. https://doi.org/10.1016/j.ijhydene.2022.07.071.

[63] Miller EC, Sherman Q, Gao Z, Voorhees PW, Barnett SA. Stability of nickel-infiltrated anodes in intermediate temperature SOFCs. ECS Transactions. 2015;68(1):1245–1254. https://doi.org/10.1149/06801.1245ecst.

[64] Khan MZ, Mehran MT, Song RH, Lee JW, Lee SB, Lim TH. A simplified approach to predict performance degradation of a solid oxide fuel cell anode. Journal of Power Sources. 2018;391:94–105. https://doi.org/10.1016/j.jpowsour.2018.04.080.

[65] Noble Tsidzi KE. The influence of foliation on point load strength anisotropy of foliated rocks. Engineering Geology. 1990;29(1):49–58. https://doi.org/10.1016/0013-7952(90)90081-b.

[66] Cheng XH, Chen HM, Chen Q. Anisotropic characterization of different materialized scaffolds: A numerical study. Biomedical Engineering Communications. 2023;2(2):12. https://doi.org/10.53388/bmec2023012.

[67] Tabei SA, Sheidaei A, Baniassadi M, Pourboghrat F, Garmestani H. Microstructure reconstruction and homogenization of porous Ni-YSZ composites for temperature dependent properties. Journal of Power Sources. 2013;235:74–80. https://doi.org/10.1016/j.jpowsour.2013.02.003.

[68] Galinski H, Bieberle-Hütter A, Rupp JLM, Gauckler LJ. Nonlinear oxidation kinetics of nickel cermets. Acta Materialia. 2011;59(16):6239–6245. https://doi.org/10.1016/j.actamat.2011.06.032.